Progress Report No. 2-5, March 31, 2000
The Home Automation and Healthcare Consortium

Analysis of the Influence of Displacement on Finger Photoplethysmography for Wearable Health Monitoring Sensors

Harry H. Asada
Principal Investigator

ABSTRACT

The ring sensor is a miniaturized, telemetric, monitoring device worn by a patient as a finger ring. The ring encapsulates photoplethysmographic, pulse oximetry combined with wireless communication and miniaturization technologies. This report describes the development of an opto-physiological model of a finger in conjunction with a ring-type photoplethysmography device (the Ring Sensor). This model is a combination of an optical model, a mechanical model, a skin capillary model and the arterial wall dynamics. It describes the photoplethysmographic effects due to the relative displacement and rotation of a finger to a ring-type opto-electric device that monitors the arterial pulsation noninvasively and continuously. Numerical simulations and experiments were conducted to verify and evaluate this model. Extensive finite element analysis was conducted, and its results were compared with the model. Based on this analysis, the advantage of isolating ring sensor was verified by FEM.

d'Arbeloff Laboratory for Information Systems and Technology
MIT

1 INTRODUCTION

The ring sensor is a miniaturized, telemetric, monitoring device worn by a patient as a finger ring. The ring encapsulates photoplethysmographic, pulse oximetry combined with wireless communication and miniaturization technologies. This device optically captures the pulsation and oxygen saturation of the arterial blood flow, and transmits the signals to a host computer via a RF transmitter. Figure 1 shows a conceptual diagram of the ring sensor [1][2]. The ring sensor consists of optoelectronic components, a CPU, a RF transmitter, a battery, and a ring chassis. The optoelectronic components, i.e. micro photodiodes and LEDs, detect the blood volume waveforms and oxygen saturation level at the patient's digital artery. The CPU controls the LED lighting sequence as well as the data acquisition and transmission process. These signals are locally processed by the on-board CPU and transmitted to a host computer for diagnosis of the patient's cardiovascular conditions. The ring sensor is completely wireless and miniaturized so that the patient can wear the device comfortably twenty-four hours a day.

This miniaturized sensor in a ring configuration is a rational design choice for twenty-four hour continuous monitoring, since a finger ring is probably the only thing that a majority of people will be willing to wear at all times. Other personal ornaments and portable instruments, such as earrings and wristwatches, are not continually worn in daily living. When taking a shower, for example, people remove wristwatches. Bathrooms, however, are one of the most dangerous places in the home. Many thousands of people, mostly hypertensives and the elderly, die in bathrooms every year. Miniature ring sensors provide a promising approach to guarantee the monitoring of a patient at all times. Also, a ring configuration provides the anatomical advantage of having transparent skin and tissue at the finger compared with other parts of the body so that it is feasible to monitor arterial blood volume at the finger base using an optoelectronic sensor. Subsequently, a variety of simple cardiac and circulatory disorders may be detected by monitoring arterial blood volume at the finger base.

In this report, we first examine and categorize a variety of movements that influence photoplethysmographic signals of the ring sensor. To articulate and analyze the influence of each movement, we build a mathematical model of the finger photoplethysmography. The main feature of the model is the integration of multiple domains such as the ring mechanics, finger tissue kinematics, digital arterial wall dynamics and biomechanical optics. Especially, the nonlinear

behavior of the arterial wall to external pressure, which is the basis of the oscillometric method of blood pressure measurement, is intensively addressed. Also, the optical property of the finger tissue is profoundly discussed. The resultant opto-physiological model of the finger and the ring sensor allows simulation of the influence of mechanical displacement of the finger on photoplethysmographic signals. Extensive simulation is conducted and the numerical results are compared with the experimental data for the validation of the model at the end. Finally, the advantage of "Isolating Ring Sensor" design shown in Figure 2 is analyzed and verified through finite element analysis.

2 APPROACH

One of the most important issues of wearable sensors is the reduction of noise caused by motion artifacts. Many kinds of motion artifacts such as fast and vivid motion of the finger, static relative displacement, and rotation of the ring relative to the finger can interfere with the measurement of the Ring Sensor. However, since the Ring Sensor is mainly to be worn by elderly patients and potential patients of cardiovascular disorders, it is reasonable to assume that the static displacement or rotation of the ring is dominant over fast movements with large accelerations. For example, if any external static force is applied to the ring so that the center point of the ring deviates from that of the finger, the photoplethysmographic signal will change. The rotation of the ring around the finger will also cause a change in the signal. A mathematical model of the finger and the ring will be very useful in understanding and analyzing the variation of the photoplethysmographic signal due to the displacement and the rotation of the ring. This model has to integrate all of the optical, mechanical and physiological properties of the Ring Sensor. In other words, the optics of the finger tissue and blood, finger tissue kinematics, geometry of the ring, and dynamics of the arteries and the capillaries must all be incorporated into one model to describe the photoplethysmographic behavior. Especially, the dynamics of the arterial wall should be modeled carefully since the compliance of the arterial wall exhibits nonlinear behavior [3]. The modeling of the optical properties is another point that has to be dealt with great care.

Figure 3 shows a cross-sectional view of the finger. The cross section of a finger is assumed to be a circle when there are no external forces. Although there are four digital arteries in the finger, we only describe two proper palmar digital arteries in this model since dorsal digital arteries are located

where the coefficients A and B are given respectively,

$$A = \frac{2\sinh(\tilde{k}R)}{(\tilde{k}R)} + \tilde{k}R\sinh(\tilde{k}R) - 2\cosh(\tilde{k}R) \tag{8}$$

$$B = \cosh(\tilde{k}R) - \frac{\sinh(\tilde{k}R)}{(\tilde{k}R)} \tag{9}$$

m_a : Absorption coefficient of tissue (a combination of absorption coefficients of whole blood and blood–free tissue : determined by the volume fraction of blood in the tissue)

m_s': Transport scattering coefficient of tissue (a combination of absorption coefficients of whole blood and blood–free tissue : determined by the volume fraction of blood in the tissue)

$\tilde{m}_a$: Absorption coefficient of blood

$\tilde{m}_s'$: Transport scattering coefficient of blood

D: Diffusion constant of tissue $(=1/[3(m_a + m_s')])$

$\tilde{D}$: Diffusion constant of blood $(=1/[3(\tilde{m}_a + \tilde{m}_s')])$

k :Inverse diffusive absorption distance of tissue $(=(m_a / D)^{1/2})$

$\tilde{k}$:Inverse diffusive absorption distance of blood $\left(=(\tilde{m}_a / \tilde{D})^{1/2}\right)$

Detailed derivations of Eqs. (1)~(9) can be found in [5].

As the absorption coefficient of blood is larger than that of tissue, the DC value of *J* increases as the two arteries are located farther from the origin, since more photons reach the detector without passing through the digital arteries. It is also natural that *J* increases as the radii of the arteries decrease. However, the amplitude of the AC component of *J* decreases as the distance of the arteries from the origin increases, since the change of the diameters of the arteries (which eventually results in the change of the extent of photon absorption) at distant locations does not give significant influence on the photons that reach the detector.

3.2 Tissue Mechanical Model

3 MODELING

3.1 Optical Model

The light emitted from the LED passes into the tissue and the number of the paths of photons is almost infinite, which makes it difficult to obtain a good optical model. The light absorption, multiple scattering, and diffusion processes all occur at the same time. It is known that the average photon migration path in the tissue is a banana shape. Assuming that the tissue is optically homogeneous, the cross section of a finger can be divided into four regions : two digital arteries, capillaries, veins, and all other regions (We will generically call these regions “blood-free tissue.”) The blood that flows in the arteries has different optical properties from those of the tissue. Looking at the cross section of the finger, it is possible to consider the digital arteries as two circular regions with different optical properties from the surrounding material. Using the analogy with electrostatics, the photon flux density at the detector can be expressed as a function of the positions of the two arteries, radii of the arteries, the position of the photodetector, and the optical properties of the tissue and the blood. Feng, S., Zeng, F., and Chance, B. derived an analytical formulation of the photon path distributions in the presence of a spherical region with different absorption and scattering properties from the surroundings in semi-infinite geometry [5]. Figure 4 shows the geometry of the light source, the photodetector, the arteries and the capillary layer. The light source is in the steady-state condition (constant source intensity of light S_0) and is located at the origin $\mathbf{r_0}=(0,0)$ of the x-y coordinate. The photon flux density at the detector which is located at $\mathbf{r_d}=(l,0)$ is denoted as J. Although the LED and the photodetector are placed along a circular ring surface, it is assumed that they are located on a straight line $y=0$. This assumption is valid as long as l is much smaller than the internal perimeter of the ring. The pulsation of capillaries is counted by dynamic change of the optical properties of the tissue surrounding the arteries. Under the assumption that the capillaries are uniformly distributed in the tissue, these optical properties are determined by the fraction of whole blood in the tissue. Since both the absorption and scattering coefficients of blood are larger than those of blood-free tissue, the combined optical coefficients generally increase at systole, resulting in decrease of the photon flux density at the photodetector. The blood in the vein also contributes to the variation of the optical coefficients of the tissue. However, it only gives influence on DC part of the variation since the AC part of venous pulsation is much smaller than that of arteries and capillaries. From this insight, the effect of venous blood is included as a DC-

level modulation factor of the optical constants of the tissue, and the effect of volumetric concentration of veins similar to the arteries is neglected in this model. Consequently, the overall optical constants of the tissue must be determined based on the fractions of blood-free tissue, blood in the capillaries, and blood in the veins.

In the analogy with electrostatics, the arteries are similar to the dielectric material in the electrical field. Noting the presence of two digital arteries which are located at $\mathbf{r_1}=(x_1, y_1)$ and $\mathbf{r_2}=(x_2, y_2)$ with radii of R_{r1} and R_{r2} respectively, the relationship between the light intensity S_0 and the photon flux density J at the detector is described as follows.

$$J = \frac{y_0 S_0}{2p}\left(\frac{k}{l^2}+\frac{1}{l^3}\right)\exp(-kl) + J_1(\mathbf{r}_1, R_{r1}) + J_1(\mathbf{r}_2, R_{r2}) \tag{1}$$

where the function $J_1(\mathbf{r},R)$ is as follows.

$$\begin{aligned} J_1(\mathbf{r}, R) &= 2Dq(R)\frac{(k|\mathbf{f}|+1)y}{|\mathbf{f}|^3}\exp(-k|\mathbf{f}|)\Phi_0(\mathbf{r}) \\ &\quad - 2Dq(R)\left\{\frac{[\mathbf{f}\cdot\mathbf{E_0}(\mathbf{r})](k|\mathbf{f}|+3)y}{|\mathbf{f}|^5} - \frac{{E_0}^y(\mathbf{r})}{|\mathbf{f}|^3}\right\}\exp(-k|\mathbf{f}|) \end{aligned} \tag{2}$$

where

$$\mathbf{r} = (x, y), \quad \mathbf{f} = \mathbf{r} - \mathbf{r_d} \tag{3}$$

$$\Phi_0(\mathbf{r}) = \frac{y_0 y S_0'}{2pD}\frac{(k|\mathbf{r}|+1)}{|\mathbf{r}|^3}\exp(-k\mathbf{r}) \tag{4}$$

where $y_0 = 0.7/m_s'$,

$$\begin{aligned} \mathbf{E}_0(\mathbf{r}) &= \left({E_0}^x, {E_0}^y\right) \\ &= \frac{y_0 S_0}{2pD}\left(\frac{3ky\mathbf{r}}{|\mathbf{r}|^4}+\frac{3y\mathbf{r}}{|\mathbf{r}|^5}-\frac{k\hat{y}}{|\mathbf{r}|^2}-\frac{\hat{y}}{|\mathbf{r}|^3}+\frac{k^2 y\mathbf{r}}{|\mathbf{r}|^3}\right)\exp(-k|\mathbf{r}|) \end{aligned} \tag{5}$$

$$q(R) = -R\exp(kR)\left\{\frac{\tilde{D}B(1-m_a/\tilde{m}_a)}{D(1+kR)\sinh(\tilde{k}R)/(\tilde{k}R)+\tilde{D}B}\right\} \tag{6}$$

$$p(R) = R^3\exp(kR)\left\{\frac{\tilde{D}A - DB}{\tilde{D}A(1+kR)+DB\left[2+2kR+(kR)^2\right]}\right\} \tag{7}$$

where the coefficients A and B are given respectively,

$$A = \frac{2\sinh(\tilde{k}R)}{(\tilde{k}R)} + \tilde{k}R\sinh(\tilde{k}R) - 2\cosh(\tilde{k}R) \tag{8}$$

$$B = \cosh(\tilde{k}R) - \frac{\sinh(\tilde{k}R)}{(\tilde{k}R)} \tag{9}$$

μ_a : Absorption coefficient of tissue (a combination of absorption coefficients of whole blood and blood–free tissue : determined by the volume fraction of blood in the tissue)

μ_s': Transport scattering coefficient of tissue (a combination of absorption coefficients of whole blood and blood–free tissue : determined by the volume fraction of blood in the tissue)

$\tilde{\mu}_a$: Absorption coefficient of blood

$\tilde{\mu}_s'$: Transport scattering coefficient of blood

D: Diffusion constant of tissue $\left(=1/[3(\mu_a + \mu_s')]\right)$

$\tilde{D}$: Diffusion constant of blood $\left(=1/[3(\tilde{\mu}_a + \tilde{\mu}_s')]\right)$

k :Inverse diffusive absorption distance of tissue $\left(=(\mu_a / D)^{1/2}\right)$

$\tilde{k}$:Inverse diffusive absorption distance of blood $\left(=\left(\tilde{\mu}_a / \tilde{D}\right)^{1/2}\right)$

Detailed derivations of Eqs. (1)~(9) can be found in [5].

As the absorption coefficient of blood is larger than that of tissue, the DC value of *J* increases as the two arteries are located farther from the origin, since more photons reach the detector without passing through the digital arteries. It is also natural that *J* increases as the radii of the arteries decrease. However, the amplitude of the AC component of *J* decreases as the distance of the arteries from the origin increases, since the change of the diameters of the arteries (which eventually results in the change of the extent of photon absorption) at distant locations does not give significant influence on the photons that reach the detector.

The initial shape of the ring is shown in Figure 5(a). The LED and the detector are placed such that their mid-point is at an angle q_1 (rad) from the horizontal axis, and both the LED and the detector are at an angle q_2 (rad) from the radial line that intersects the mid point. As the finger moves inside the ring, the pressure at the contact point increases and both the finger tissue and the compliant material inside the ring go through deformation. This is shown in Figure 5(b).

O is the center of the ring and *c* is the reference point (initial center pint) of the finger located at the bone. As the reference point of finger moves by displacement *d* at an angle *a*,. the distance *r* (represented as a function of *g*) from the reference point of the finger to the skin changes from its initial value r_0. At the same time, the compliant material inside the ring also deforms and the distance *R* (represented as a function of *q*) from the center of the ring to the ring inner material also deviates from its initial value R_0. Denoting the pressure at the contact as *P*, we can get the force equilibrium equation,

$$\begin{aligned} &P(q) = [r_0 - r]k_t = [R - R_0]k_b \\ &P(q) \geq 0, \textit{ always} \Rightarrow r \leq r_0 \textit{ and } R \geq R_0, \textit{ always} \\ &P(g) = [r_0 - r(g)]k_t \quad : P \text{ as a function of } g \\ &P(q) = [R(q) - R_0]k_b \; : P \text{ as a function of } q \end{aligned} \tag{10}$$

where k_t is the stiffness of the finger tissue and k_b is the stiffness of the compliant material inside the ring. From Eq. (10), we can get the following relationship.

$$R = R_0 + (r_0 - r)\left(\frac{k_t}{k_b}\right) \tag{11}$$

From the kinematics of the tissue, we can also get the following equations.

$$r^2 = R^2 + d^2 - 2Rd\cos(a - q) \tag{12}$$

$$R^2 = r^2 + d^2 - 2rd\cos(p - (a - g)) \tag{13}$$

Combining Eqs. (11), (12), and (13), the information about the deformation of the finger tissue and the ring inner material is obtained.

$$R(q) = \frac{(r_0 + R_0)^2 - d^2}{2[R_0 + r_0 - d\cos(a - q)]} \quad if \;\; k_b = k_t \tag{14a}$$

$$R(q) = \frac{b - \sqrt{b^2 - ac}}{a} \quad if \;\; k_b \neq k_t \tag{14b}$$

where,

$$a = \left(\frac{k_b}{k_t}\right)^2 - 1$$

$$b = R_0\left(\frac{k_b}{k_t}\right)^2 + r_0\left(\frac{k_b}{k_t}\right) - d\cos(a - q)$$

$$c = {r_0}^2 + {R_0}^2\left(\frac{k_b}{k_t}\right)^2 + 2R_0 r_0\left(\frac{k_b}{k_t}\right) - d^2$$

and,

$$r(g) = \frac{(r_0 + R_0)^2 - d^2}{2[R_0 + r_0 + d\cos(a - g)]} \quad if \;\; k_b = k_t \tag{15a}$$

$$r(g) = \frac{b' - \sqrt{b'^2 - a'c'}}{a'} \quad if \;\; k_b \neq k_t \tag{15b}$$

where,

$$a' = \left(\frac{k_t}{k_b}\right)^2 - 1$$

$$b' = R_0\left(\frac{k_t}{k_b}\right) + r_0\left(\frac{k_t}{k_b}\right)^2 + d\cos(a - g)$$

$$c' = {R_0}^2 + {r_0}^2\left(\frac{k_t}{k_b}\right)^2 + 2R_0 r_0\left(\frac{k_t}{k_b}\right) - d^2$$

As shown in Figure 6, the location of the artery 1 which is $\mathbf{r_1}=(x_1,y_1)$ in the optical model given by Eq. (1), can be derived using simple kinematics.

$$x_1 = d\sin[a - (q_1 - q_2)] + h_1\sin[b + (q_1 - q_2)] \quad (16a)$$

$$y_1 = R_1 - d\cos[a - (q_1 - q_2)] + h_1\cos[b + (q_1 - q_2)] \quad (16b)$$

where,

$R_1 = R(q_1 - q_2)$ from Eqs. (14a) and (14b)

$$h_1 = h_0\left(\frac{r_1}{r_0}\right)$$

where,

$r_1 = r(p - b)$, from Eqs. (15a) and (15b)

The location of the artery 2 which is $\mathbf{r_2}=(x_2,y_2)$ can also be obtained using similar derivations.

3.3 Dynamics of the Arterial Wall

The compliance of the arterial wall changes nonlinearly. There are many factors that influence the arterial wall compliance [17][18], such as temperature, pressure, age, or even emotion of the person. Among them, pressure is one of the most sensitive factors that change the compliance dramatically. Depending on the transmural pressure P_t, which is defined as the difference between the internal pressure P_i and external pressure P_o, the diameter changes of the digital artery differ even with the same change in blood pressure. Figure 7 shows the relationship between the arterial wall radius R_r and the transmural pressure P_t [3][18][19][20][21]. As shown in the figure, even with the same change of transmural pressure DP_t, the change of the arterial radii, DR_{r1} and DR_{r2}, are different depending on the operating point of P_t. The maximum arterial pulsation occurs approximately when

the transmural pressure is zero. After this point, the arterial pulsation begins to diminish since the artery becomes occluded by the excessive external pressure [3][19]. This is a well-known principle used in oscillometric blood pressure measurement devices.

The internal pressure of the artery, which is actually what we define as “blood pressure”, is not actively controllable. However, we can change the amplitude of the volumetric pulsation of the artery by changing the external pressure P_o even under the same blood pressure. In our ring configuration, as the displacement d increases, the pressure around the contact point increases. This also changes the pressure applied to the digital arteries depending on the configuration and position of the ring. To calculate the radii of the arteries (R_{r1} and R_{r2} in Eq. (1)), $P(\gamma)$ when $\gamma=\pi-\beta$ and $\gamma=\beta$ must be calculated from Eq. (10), and this becomes the external pressure P_{o1} and P_{o2} applied to digital artery 1 and 2 respectively.

Wesseling *et al* measured pressure-diameter relationships of segments of human finger arteries *in vitro* [22]. Figure 19 shows their experiment results. The figure clearly shows that there is a steep slope in the collapse region near zero transmural pressure. According to the experiment, inner diameter of human digital arteries is approximately 0.8 mm when fully expanded. Considering that there are four digital arteries and two of them (dorsal digital arteries) are smaller than the other two (proper palmar digital arteries), total volume of fully-expanded digital arteries in 1 cm finger segment is 0.015 ml, which agrees with the conjecture made in the previous section.

In this approach, we model the relationship of R_r and P_t as a sigmoid function for simplicity.

$$R_r = \frac{C_1}{1+\exp\left(-C_2\left(P_t - C_3\right)\right)} \quad \text{(mm)} \tag{17}$$

where

$P_t = P_i - P_o$

P_i : *blood pressure inside artery*

P_0 : *pressure outside of artery*

R_r : *radius of digital artery*

Fitting this sigmoid function with the pressure-diameter relation curve in Figure 19, three constants can be determined as follows.

$$C_1 = 0.4,\ C_2 = 0.15,\ C_3 = 0$$

The plot of this artery model is shown in Figure 22.

Finally, R_{r1} and R_{r2} in Eq. (1) can be described as follows.

$$R_{r1} = R_r\left(P_i - P_{01}\right) \tag{18a}$$

$$R_{r2} = R_r\left(P_i - P_{02}\right) \tag{18b}$$

where,

$P_{01} = (r_0 - r_1)k_t$, $P_{02} = (r_0 - r_2)k_t$, from Eq. (10)

where,

$r_1 = r(p - b)$, $r_2 = r(b)$, from Eqs. (15a) and (15b)

3.4 Parameter Calibration and Estimation

3.4.1 Validation of the Model and Determination of Stiffness of the Tissue by FEM

The value of k_t should be determined for the said tissue mechanics model. Although human tissue is a nonlinear, inhomogeneous, anisotropic material, its behavior has been successfully described by isotropic, homogeneous and incompressible constitutive relations. [6][7][8]. Since the finger cross section is modeled as a group of elastic springs extending in radial direction in this research, the stiffness of finger tissue has to be determined. The approach used in this research was to simulate the mechanical deformation of finger by finite element analysis (FEM), and then find the best value of k_b that describes the closest behavior to the FEM result.

Many researchers used finite element method to describe the behavior of the human tissue [6][7][8][9][10]. Kamm *et al* conducted analysis of tissue deformation in the lower leg [6]. He found out that the Young's modulus is about 1.2×10^4 (Pa) in the lower leg. Raju conducted FEM of

the fingertip and he divided the fingertip by 5 different layers with different mechanical properties [9]. The range of the Young's modulus he used for the layers was around 10^3~10^4. Maeno analyzed the contact problem between an elastic finger having a curved surface and an object [7]. He used a rather high elastic modulus of 10^6. Although a number of publications described about the elastic modulus of human tissues, no value of for the elastic modulus of finger base could be found. Though, there were some researchers who reported experiment results about volumetric changes of finger segment under a controlled external pressure. Yamakoshi *et al* [11] reported an interesting experiment result about the volumetric change of finger segment. They placed a cuff around the finger segment, and monitored the volumetric change of the finger segment while increasing the cuff pressure. They reported that about 0.26 ml of volume change occurred in 1 cm finger segment when he applied 120 mmHg cuff pressure around the finger.

Based on their experiment result, we used an indirect approach to estimate the elastic modulus of finger. We simulated Yamakoshi's experiment with the finite element method with different values for the Young's modulus of the tissue. The value for modulus that produced the closest agreement with the experiment result was employed in the finger model verification. Kamm *et al* [6] used the similar approach in estimating Young's modulus of lower legs. Figure 25 and Figure 26 shows the finite element model used in this process. The FEM analysis was conducted with commercial software (ADINA Version 7.3.2, ADINA, Inc. Watertown, MA). The finger segment was simplified to be a cylinder of 2 cm diameter with 5cm length. A uniform pressure of 120 mmHg was given on the surface of the cylinder on a 3 cm segment. This length is the same as that of the finger cuff used by Yamakoshi. Multiple 3-D simulations with different Young's modulus were conducted, and the volumetric change for each simulation was measured. Resembling Yamakoshi's experiment, the volumetric change was measured only in 1 cm segment in the center. Figure 21 shows the volumetric changes of the finger segment with various values for Young's modulus generated by FEM. This analysis shows that the volumetric change is closest to the expected value of 0.26 ml when Young's modulus of 2.0×10^4 (Pa) was chosen. Using this value, another 3-D finite element analysis was conducted. Figure 27 is the schematic of the FEM analysis when the finger ring moved downward (external force from θ=90 degree), and Figure 28 is the same FEM analysis when the finger ring is moved to the side. (external force from θ=20 degree). Figure 29 and Figure 30 shows the two simulation results of deformed finger cross section. The finger diameter is 2 cm and the length of the segment is 4 cm. The width of the ring is 1 cm. The ring was given a displacement of 2

mm from the top. The FEM simulation result in Figure 30 shows that the contour lines of the pressure roughly lie in the radial direction. This means that our radial-spring assumption of the finger tissue behavior is actually quite good. While trying to fit the value of k_t to FEM analysis result, it was also found that the spring constant should vary depending on the angle. This is mainly due to the fact that the thickness of the tissue (distance from the skin to the surface of the bone) is not uniform with the angle. Fitting the spring constant of the tissue from this analysis, k_t is determined to be as follows.

$$k_t(q) = 25\cos\left(q + \frac{p}{2}\right) + 64 \qquad (mmHg/mm) \tag{19}$$

where q is the angle of the tissue of interest. This value of k_t will be used in the numerical simulation of the whole model.

3.4.2 Determination of Optical Properties : Capillaries and Veins

Since the tissue is assumed to be a homogeneous composite of blood-free tissue, whole blood in capillaries, and blood in veins, the absorption and scattering constants of the tissue are expressed in terms of the coefficients of blood-free tissue and whole blood, and the volume fractions of the three materials.

$$m_a = \frac{\tilde{m}_{at} V_t + \tilde{m}_a (V_c + V_v)}{V_t + V_c + V_v} \tag{20a}$$

$$m_s' = \frac{\tilde{m}_{st}' V_t + \tilde{m}_s' (V_c + V_v)}{V_t + V_c + V_v} \tag{20b}$$

m_a : Overall absorption coefficient of the tissue

$\tilde{m}_{at}$: Absorption coefficient of blood-free tissue

$\tilde{m}_a$: Absorption coefficient of whole blood

m_s' : Overall transport scattering coefficient of the tissue

$\tilde{m}_{st}'$: Transport scattering coefficient of blood-free tissue

$\tilde{m}_{s}'$: Transport scattering coefficient of whole blood

V_t: Volume of the blood-free tissue

V_c: Volume of the whole blood in capillaries and small artery branches

V_v: Volume of the whole blood in veins

According to [4], the conventional values of $\tilde{m}_{at}$ and $\tilde{m}_{st}'$ are 0.03 /mm and 1.0 /mm, respectively. $\tilde{m}_a$ and $\tilde{m}_s'$ can be also calculated as,

$$\tilde{m}_a = s_a r \tag{21a}$$

$$\tilde{m}_s' = \bar{s}_s r(1-\mathrm{HCT}) \tag{21b}$$

where s_s is the backscattering cross section, and s_a is the absorption cross section of red blood cells. HCT is the blood hematocrit (~0.45), and r is the red-cell density. $r = \mathrm{HCT}/V$ where $V(=87\times10^{-9}\,\mathrm{mm}^3)$ is the red-cell volume. Conventional value of s_s is $0.558\times10^{-6}\,\mathrm{mm}^2$ [4] and s_a can be calculated as,

$$s_a = s_{ao}(\mathrm{OS_T}) + s_{ar}(1-\mathrm{OS_T}) \tag{22}$$

where $\mathrm{OS_T}$ is oxygen saturation (~0.95 typically) and s_{ao} and s_{ar} can be obtained for various light wavelengths from [12]. For λ=660nm (red light), s_{ao} and s_{ar} are around 0.044×10^{-6} (mm^2) and 0.455×10^{-6} (mm^2), respectively. For λ=950nm (IR light), s_{ao} and s_{ar} are around 0.173×10^{-6} (mm^2) and 0.102×10^{-6} (mm^2), respectively. As a result, $\tilde{m}_s'$ is 1.59 /mm, and $\tilde{m}_a$ is 0.334 /mm (λ=660nm) or 0.877 /mm (λ=950nm). These values are also in good agreement with the range of absorption and scattering coefficients of human tissue suggested by [13] and [14].

To get the overall optical properties of the tissue, the volumes of the components (i.e. blood-free tissue, whole blood in capillaries, and whole blood in the veins) should be found. Although no values for the volume fractions of these components in the finger cross section could be found in the literature, they can be estimated from available experimental results published in the literature. Yamakoshi *et al.* [11] measured the volume change of a middle finger as the pressure in the cuff placed around the finger increased (Figure 20). They reported that the finger volume decreased by 0.26 ml in 1cm finger segment as the cuff pressure increased from 0 to around 150 mmHg. At this cuff pressure, it is certain that even digital arteries would be occluded. If we assume that this finger volume decrease of 0.26 ml is mainly due to the absence of blood (i.e. the blood is "squeezed" out of the finger segment.), we can say that the volume of the blood in the segment was originally 0.26 ml. They also reported that the AC part of the volume change was maximum at around 90 mmHg, corresponding to the mean arterial pressure, and the maximum volume change was 0.015 ml. Noting that capillaries and veins are already occluded at this high pressure, we can say that this amplitude is the volumetric change of the blood in the digital arteries (two proper palmar digital arteries and two dorsal digital arteries). Their experiment results also showed that approximately half of the volume change occurs in the lower pressure range. After this point, the slope of volume change becomes less stiff. Yamakoshi *et al.* [15] measured this inflection point, and suggested that it corresponds to the highest venous pressure. Therefore, it can be said that the capillary occlusion begins approximately from this inflection point. Yamakoshi measured this inflection point from several subjects and estimated it to be around 15 mmHg.

From these arguments, about half of the blood in the finger segment can be considered to be venous blood (including venulus), and the other half consists of capillary and arterial blood. From the experiment result of [11], the total volume of the blood in the four digital arteries represents only about 5 percent of the whole blood in the finger segment. Considering that about half the blood in the cross section is venous blood, approximately 45% of the blood resides in capillaries and arterioles other than four digital arteries. In the same experimental result, it was shown that the volumetric change of the finger segment at low pressure was about 0.003 ml. Unlike the digital arteries that show continuous volume change with pressure, capillaries are thought of as on-off type tubes. The number of the occluded capillaries increases as the external pressure increases. In this case, we can model the pulsating volume of whole blood in capillaries and small arterioles (V_c) as a function of arterial blood pressure. Its DC value can be modeled as a linear decreasing function of

external pressure, where its AC part is synchronized with arterial blood pressure pulsation with amplitude of approximately 3 percent (0.003/0.11) of its DC part. V_c is considered to be zero after P_{as} as is shown in the experiment result of [11]. Since the capillary pressure value in the arteriolar end is 30.6~34.3 mmHg [16], most of the capillaries are occluded in the higher pressure range (>~40 mmHg). After about 40 mmHg, V_c is mostly the volume of arterioles and small artery branches, and volumetric pulsation occurs mostly due to the arteries and arterioles.

$$
\begin{aligned}
V_c &= a\left[\left(\frac{P_a - P_{am}}{P_{as} - P_{ad}}\right)\times 0.03 + 1\right] && (ml) \quad when\ P_o < P_{\inf} \\
V_c &= b\left(\frac{P_{as} - P_o}{P_{as} - P_{\inf}}\right)\left[\left(\frac{P_a - P_{am}}{P_{as} - P_{ad}}\right)\left(\frac{P_{ad} - P_o}{P_{ad} - P_{\inf}}\right)\times 0.03 + 1\right] && (ml) \quad when\ P_{\inf} < P_o < P_{ad} \\
V_c &= c\left(\frac{P_{as} - P_o}{P_{as} - P_{\inf}}\right) && (ml) \quad when\ P_{ad} < P_o < P_{as} \\
V_c &= 0 && (ml) \quad when\ P_o > P_{as}
\end{aligned}
\tag{23}
$$

P_a : Arterial Blood Pressure

P_m : Mean arterial blood pressure

P_{as} : Systolic arterial pressure

P_{ad} : Diastolic arterial pressure

P_o : Pressure applied from outside

P_{inf} : Pressure at inflection point

Fitting the constants *a*, *b*, and *c* with the curve in Figure 20, we can get $a = b = c = 0.12$. From the above argument, it is also clear that V_v is decreasing from 0.13 ml to zero with external pressure ranging from 0 to P_{inf}.

$$
\begin{aligned}
V_v &= 0.13\frac{(P_{\inf} - P_o)}{P_{\inf}} && (ml) \quad P_o < P_{\inf} \\
V_v &= 0 && (ml) \quad P_o > P_{\inf}
\end{aligned}
\tag{24}
$$

and,

$$V_t = pR^2 - 0.26 \quad (ml) \tag{25}$$

where R is the radius of finger cross section (~1 cm). The total volume of the 1cm length finger segment will be,

$$V = V_t + V_c + V_v + V_a \tag{26}$$

where V is the total volume and V_a is the blood volume in digital arteries. V_a will be determined by arterial dynamics model in next section.

Unlike the case of cuff pressure, P_o is not uniform around the finger in ring sensor configuration. This means that the optical properties of the tissue are not uniform in the finger cross section. Since the important optical properties are those around sensing area, the pressure around optical sensors can be used for P_o in this model.

3.5 Completing the model

Now that we have a model for digital artery, we can do simulation of the volumetric change of the finger segment as a function of external pressure by using Eq. (26). Figure 23 and Figure 24 shows the result of the numerical simulation. The heart rate was set to be 90 /min, and blood pressure was set to be 120/90. From the figure, it is clear that the AC part of the volumetric change of blood becomes the maximum around the mean blood pressure. However, it is also seen that the exact maximum point of the simulation is less than actual mean blood pressure by 5~10 mmHg. This fact has been reported by many researchers [3]. This is one of the well-known defects of oscillometric pressure monitoring method. The DC part of the simulation result agrees well with actual experiment result shown in Figure 20.

The tissue mechanical model and blood vessel models have been verified by FEM and known experiment results. Combining the mechanical model describing the locations of the two arteries, the arterial wall dynamics equations given by Eqs. (26a) and (26b), and the optical model equations given by Eqs. (1), (20a), and (20b), the whole model is completed.

4 NUMERICAL SIMULATION OF THE COMPLETE MODEL AND VERIFICATION BY FINITE ELEMENT METHOD AND EXPERIMENT

Numerical simulations and experiments were conducted with different angles of movements. The numerical simulations were performed using MATLAB version 5.2. The first case (Figure 8(a)) is when the direction of movement is aligned with that of a digital artery. In the second case (Figure 8(b)), the finger moves in the direction of the mid-point of two digital arteries. In the numerical simulations, the blood pressure (internal pressure P_i) is given as a combination of two sinusoidal functions, one with a frequency of 1.2 Hz and the other 2.4 Hz. By this combination, we can closely simulate the two-peak feature of a real heart beat. For the optical coefficients, the values of $\tilde{m}_a = 0.877/mm$, and $\tilde{m}_s' = 1.59/mm$ are used in the numerical simulations as was discussed in the previous sections. m_a and m_s' are determined by Eqs. (20a) and (20b). In the experiments, the LED and the photodetector are closely packed in a sensor unit board, and the ring is positioned so that the sensor is aligned in the direction of movement in each case. ($\alpha=q_1$)

4.1 Analysis of the Simulation and Experiment : Case 1

When the direction of finger movement is aligned with the location of a digital artery ($\alpha=\beta$), it is expected that the amplitude of the photoplethysmograph will change greatly as d (displacement) increases due to two reasons. First, as the sensor is aligned with a digital artery, the distance from the artery and the photodetector will decrease significantly as d increases. This will result in a more change of light absorption by the blood with the same change of the diameter of digital artery. Secondly, as the direction of movement is aligned with the location of a digital artery, the external pressure around the artery which is P_o will increase quickly, resulting in the maximum pulsation point of the transmural pressure more easily. This will also give a more highly pulsating signal at the photodetector. Figure 9 shows the numerical simulation of the finger and the ring configuration with a gradual increase of the displacement d. The large outer circle represents the ring, and the inner line that resembles a distorted circle is the finger surface. The two small circles inside the finger represent the two digital arteries, and the plus sign (+) inside the finger represents the reference point of the finger (which was denoted as point c in previous figures). It can be clearly seen that this reference point moves toward the direction of a digital artery as the displacement

increases, and the digital artery goes closer to the LED and the photodetector which were represented as a small square (□) and a small star (*) on the finger surface at around 20 degree respectively. The same numerical simulation was done using ADINA. Figure 28 shows the configuration, and Figure 31 and Figure 32 show the result of the FEM analysis. Figure 32 is the cut-plane view in the center. It is clearly seen that the pressure at the tissue around θ=20 degree is the maximum. Since one of two proper palmar digital arteries resides in this region, the artery will be under significant pressure, resulting in a large pulsation due to the nonlinearity of the compliance of arterial wall. The pressure around one of the digital arteries (θ=20 degree) increases as high as almost 120 mmHg as is shown in Figure 12. Figure 13 shows the pressure distribution as a function of θ calculated by FEM analysis. This curve shows similar shape as the curve in Figure 12 that was generated by the lumped parameter model, implying that our lumped parameter model is valid in calculating the pressure distribution.

From the viewpoint of the arterial wall dynamics, it is expected that the amplitude of the photoplethysmograph will increase as the relative displacement of the finger to the ring increases up to a certain point where the transmural pressure goes to zero. After that peak point, the amplitude is expected to decrease since the digital artery will begin to be occluded. The simulation results and the experiment results are shown in Figure 10 and Figure 11 respectively. The upper plots of Figure 10 and Figure 11 are the photoplethysmographs, and the bottom figures are the pressures at the sensor unit. Both results show that there is a certain point of external pressure P_o that the amplitude of the photoplethysmograph becomes the maximum. (The experiment result of case 1 shows a small oscillation even at very high external pressure. This is mainly due to the measurement noise and the signals at this region do not show the typical characteristics of human heart beats such as two-peak waveform.)

4.2 Analysis of the Simulation and Experiment : Case 2

The second case is when the direction of finger movement is towards the middle point of the two digital arteries, i.e, to the palm side ($\alpha=90^o$). In this case, the change of amplitude of the photoplethysmograph with finger displacement is not expected to be as great as in case 1 since the pressure increase at the artery is not as much as in case 1 with the same extent of displacement. In addition, as the distances of the two digital arteries from the sensor unit are geometrically longer

than those of case 1, the overall amplitude of the photoplethysmography signal will not be large. This means that the amplitude of the photoplethysmograph will not change much even though the finger moves significantly to the direction of the palm side. This conjecture is also supported by the FEM analysis shown in Figure 29 and Figure 30. Although the pressure around two digital arteries increases, it does not increase as much as the case 1. As is shown in Figure 17, the pressure around a digital artery (θ=20 degree) only increases up to 30 mmHg. With this external pressure, the digital artery will not show any significant amplitude of pulsation. The pressure-angle curve generated by FEM analysis shows a similar trend. Thus, it is expected that the amplitude of the signal will remain very small regardless of the finger displacement. The movement of the finger in the ring is graphically visualized using our model in Figure 14.

The experimental result is shown in Figure 15, and the simulation result in Figure 16. As was expected, the amplitude of the photoplethysmograph shows almost no change in experiment. In this configuration, it is even hard to recognize the pulse, in both experiment and simulation. In both results, the amplitude becomes a little larger with low pressures. This slight increase of the amplitude is from the pulsation of the capillaries on the palm side of the finger. Capillaries usually become occluded at an external pressure of around 10~35 mmHg since the internal blood pressure of the capillaries is around that range [16]. This explains the disappearance of pulsation at higher pressures in the experiment result in case 2. (Small oscillation at high external pressures is mainly measurement noise.) In other words, the photoplethysmograph of case 2 catches the pulsation from the capillaries when the external pressure is low. However, as the external pressure increases above 10~35 mmHg, this pulsation disappears as the capillaries become occluded. As the arterial pulsation cannot be apparently detected by the photoplethysmography at this configuration because the distance between the arteries and the sensor is long, we can see almost no pulsation with higher external pressures. Rather, the pulsation of the capillaries plays a major role with a low external pressure, although its amplitude is much smaller than that in case 1 in which the photoplethysmograph is mostly driven by arterial pulsation at the higher pressure. The simulation result also exhibits a similar behavior.

Although we can catch much larger pulsation by giving a high external pressure around 80~100 mmHg, it is not practical to use this kind of high pressure since it will occlude all the capillaries and block the venous return. This will result in jamming of the peripheral circulation and the finger will

fall into necrosis eventually. Therefore, it is recommended to use a lower external pressure such as 10 mmHg. In this case we will be capturing mostly capillary pulsation.

5 VERIFICATION OF ADVANTAGES OF THE ISOLATING RING SENSOR BY FINITE ELEMENT METHOD.

As was verified in the model, photoplethysmographic signal changes much depending on the pressure given on the blood vessels. From the viewpoint of physiological signal monitoring, it is not recommended that the monitored signal should fluctuate with any external disturbance. For example, if the ring sensor moves due to any external force such as the case shown in Figure 3(b), the monitored signal will vary since the pressure applied on the blood vessels change. From this argument, if the pressure change can be minimized when the same amount of displacement is applied, the signal variation will be minimized. Figure 33 and Figure 34 show the FEM model of the simplified finger segment with isolating ring sensor. Each ring has 3 mm of width and two rings are separated by 12 mm. The optical sensor unit is attached in the middle of the two rings, and the unit is mechanically decoupled from the two outer rings. Figure 35 and Figure 36 show the pressure distribution of the finger segment when the outer rings are moved by an external force from θ =90 degree. Figure 36 is the cross section of the finger segment in the middle of the two outer rings. From this figure, it is clear that the maximum pressure in this cross section is less than 1400 Pascal ($\approx$ 10.5 mmHg), although the cross section of the contact point is much more distorted and its pressure is much higher (Figure 37). Comparing this result with that of Figure 30 which has the maximum pressure of about 11150 Pascal ($\approx$ 83.8 mmHg), it is obvious that the pressure increase at the sensing point is significantly small with isolating ring configuration. In other words, when the ring is pushed by the same external pressure, the pressure variation at the sensing point is much smaller in the isolating ring sensor, and this will result in a small fluctuation of photoplethysmographic signal. This argument is also supported by comparing the other two FEM results (Figure 32 and Figure 40) which is the case that the external force is coming from θ = 20 degree. In case of the single ring configuration in Figure 32, the maximum pressure generated by the 2 mm displacement of the ring is around 18250 Pa ($\approx$ 137 mmHg), while that in case of the isolating ring sensor in Figure 40 is only around 1120 Pa ($\approx$ 8.4 mmHg). It is clear that the pressure variation is much less sensitive to external forces with isolating ring sensor.

The pressure variation by displacement of the ring body can be further reduced by making the distance between two outer rings longer. Figure 43 and Figure 44 show the FEM analysis of this case. The distance between two outer rings is 18 mm. The maximum pressure in the finger cross section in the middle is about 300 Pa (≈ 2.3 mmHg) which is even less than the case of Figure 36. Therefore, it is better to have the distance between two outer rings longer. However, there are always limitations in this approach, since the distance cannot be longer than the distance between knuckles. In addition, it is not recommended to make the distance too long since it will make this device inconvenient for people to wear for a long time. Thus, a tradeoff will be needed in the practical design of the isolating ring sensor.

6 CONCLUSIONS

A finger model for photoplethysmography of the Ring Sensor was developed. This model is an interdisciplinary physiological model that integrates an optical model, mechanical model, and the dynamics of the arteries and the capillaries. This model was verified by experiments and numerical simulations. This model is especially useful in describing the nature of the finger-based health monitoring device (the Ring Sensor). For example, from the viewpoint of noise minimization issues, there are many advantages of having this mathematical finger model in designing a ring sensor that is strong to noise caused by finger movement. As there are many design parameters that have to be tuned in the development of a ring sensor, this finger model will be a good analytic method in optimizing those parameters such as the compliance of the inner material of the ring and the configuration of the sensor. Further refinement of this model will focus on investigating the non-linearity of the finger tissue, as well as on more detailed modeling of the anatomical elements such as skin layers.

REFERENCES

[1] Rhee, S., Yang, B-H. and Asada, H., "The Ring Sensor: a New Ambulatory Wearable Sensor for Twenty-Four Hour Patient Monitoring," Proc. of the 20th Annual International Conference of the IEEE Engineering in Medicine and Biology Society, Hong Kong, Oct, 1998

[2] Rhee, S., Yang, B-H. and Asada, H., "A Twenty-Four Hour Tele-Nursing System Using a Ring Sensor," Proc. of 1998 IEEE International Conference on Robotics and Automation, Leuven,

Belgium, May, 1998

[3] Wesseling, K. H., de Wit, B., van der Hoeven, G. M. A., van Groudoever, J. and Settels, J. J., “Physiocal, Calibrating Finger Vascular Physiology for Finapres,” Homeostatis, 36 (2-3), 67-82 (1995)

[4] Takatani, S. and Graham, M.D., “Theoretical Analysis of Diffuse Reflectance from a Two-Layer Tissue Model,” IEEE Transactions on Biomedical Engineering, Vol. 26, No. 12, December 1979, 656-664

[5] Feng, S., Zeng, F. and Chance, B., “Photon Migration in the Presence of a Single Defect : a Perturbation Analysis,” Applied Optics, Vol. 34, No. 19, 3826-3837 (1995)

[6] Dai, G., Gertler, J. P. and Kamm, R. D., “The Effect of External Compression on Venous Blood Flow and Tissue Deformation in the Lower Leg,” Journal of Biomedical Engieering, December 1999, Vol. 121, 557-564

[7] Maeno, T., Kawai, T. and Kobayashi, K., “Analysis and Design of a Tactile Sensor Detecting Strain Distribution Inside an Elastic Finger,” Proceedings of the 1998 International Conference on Intelligent Robotics and Systems, Victoria, B.C., Canada 1658-1663

[8] Srinivasan, M.A. and Dandekar, K., “An Investigation of the Mechanics of Tactile Sense Using Two-Dimensional Models of the Primate Fingertip,” Journal of Biomechanical Engineering, Feb.1996, Vol. 118, 48-55

[9] Raju, B., “Encoding and Decoding of Shape in Tactile Sensing,” MS Thesis, Department of Mechanical Engineering, Massachusetts Institute of Technology, 1998

[10] Vannah, W.M.. and Childress, D.S., “Indentor tests and finite element modeling of bulk muscular tissue in vivo,” Jornal of Rehabilitation Research and Development, Vol. 33, No. 3, July 1996, pp. 239-252

[11] Shimazu, H., Kawarada, A., Ito, H. and Yamakoshi, K., “Electric Impedance cuff for the indirect measurement of blood pressure and volume elastic modulus in human limb and finger arteries,” Medical & Biological Engineering & Computing, 1989, 27,477-483

[12] Van Assendelft, O.W., “Spectrophotometry of Hemoglobin Derivatives,” Assen, The Netherlands: Royal Vangorcum, 1970, ch. 3, pp. 47-151

[13] Hull, E.L., Nichols, M.G. and Foster, T.H., “Quantitative broadband near-infrared spectroscopy of tissue-simulating phantoms containing erythrocytes,” Physics in Medicine

and Biology, 43 (1998) 3381-3404

[14] Wagnieres, G., Cheng, S., Zellweger, M., Utke, N., Braichotte, D., Ballini, J. and Bergh, H., "An optical phantom with tissue-like properties in the visible for use in PDT and fluorescence spectroscopy," Physics in Medicine and Biology, 42 (1997) 1415-1426

[15] Shimazu, H., Ito, H. and Yamakoshi, K., "Noninvasive method for estimating the mean capillary pressure and pre- and postcapillary resistance ratio in human fingers," Medical & Biological Engineering & Computing, 1986, 24,585-590

[16] Landis, E.M. and Pappenheimer, J.R., "Exchange of Substances through the capillary walls," In Handbook of Physiology, Hamilton, W.F. and Dow, P. (Eds), 1963, 961-1034

[17] Tanaka, H. and Thulesius, O., "Effect of Temperature on Finger Artery Pressure Evaluated by Volume Clamp Technique," Clinical Physiology (1993) 13, 535-545

[18] Ando, J., Kawarada, A., Shibata, M., Yamakoshi, K. and Kamiya, A., "Pressure-volume Relationships of Finger Arteries in Healthy Subjects and Patients with Coronary Atherosclerosis Measured Non-invasively by Photoelectric Plethysmography," Japanese Circulation Journal, Vol. 55, June 1991, 567-575

[19] Yamakoshi, K., Shimazu, H., Shibata, M. and Kamiya, A., "New Oscillometric Method for Indirect Measurement of Systolic and Mean Arterial Pressure in the Human Finger. Part 1 : Correlation Study," Medical & Biological Engineering & Computing (1982), 20, 307-313

[20] Raamat, R., Talts, J., Jagomagi, K. and Lansimies, E., "Methematical modeling of non-invasive oscillometric finger mean blood pressure measurement by maximum oscillation criterion," Medical & Biological Engineering & Computing, 1999, 37, 784-788

[21] Shimazu, H., Ito H., Kawarada, A., Kobayashi, H., Hiraiwa, A. and Yamakoshi, K., "Vibration technique for indirect measurement of diastolic arterial pressure in human fingers," Medical & Biological Engineering & Computing, 1989, 27,130-136

[22] Langewouters, G.J., Zwart, A., Busse, R. and Wesseling, K.H., "Pressure-diameter relation ships of segments of human finger arteries," Clinical Physics and Physiological Measurement, 1986, Vol. 7, No. 1, 43-55

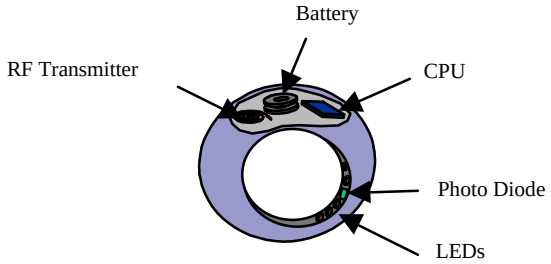

Figure 1 Conceptual diagram of the ring sensor

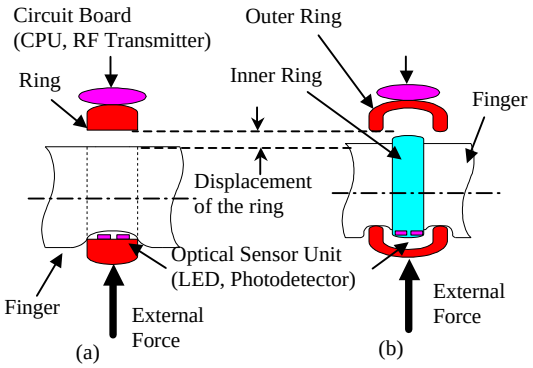

Figure 2 Dislocation of ring sensors due to external load
(a) Traditional single body design under external force
(b) New isolating ring sensor under external force

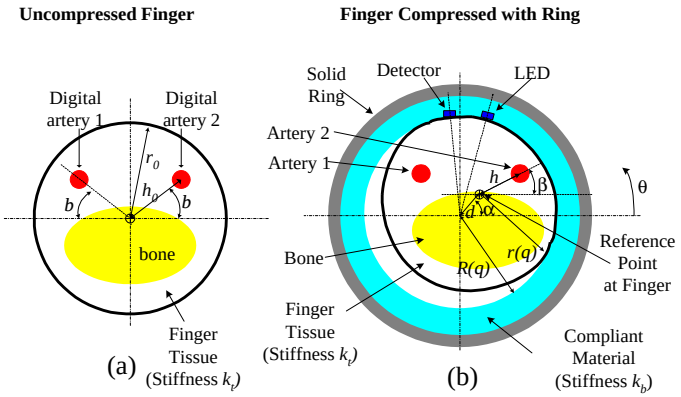

Figure 3 (a) Uncompressed finger under no external force (d=0). (b) Finger compressed by the ring due to an external force.(d>0)

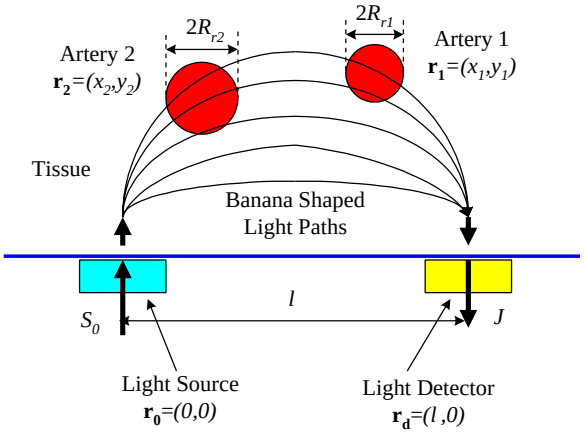

Figure 4 Optical model of the finger and optical elements. Blood vessels have different optical properties from the tissue.

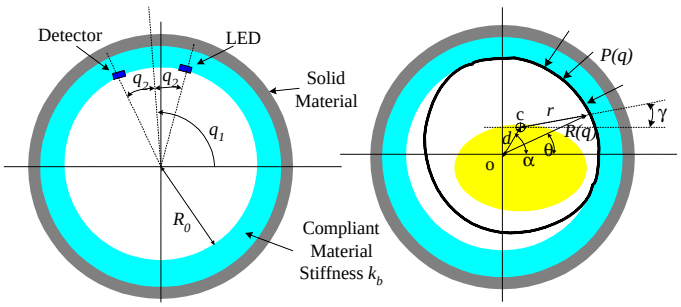

Figure 5 (a) Initial state of the ring with LED and photodetector (b) When the finger moves in the ring (Finger tissue is deformed.)

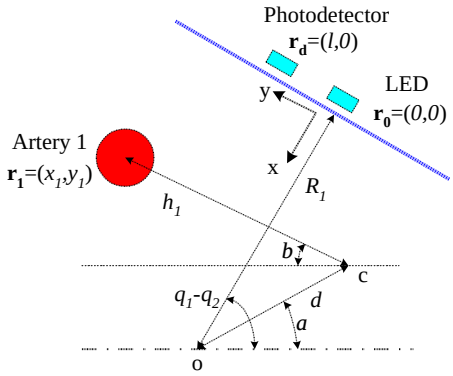

Figure 6 Geometry of the LED, the photodetector, the artery 1, and the skin capillary layer

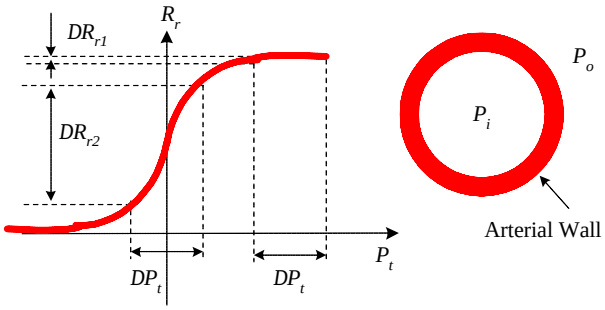

Figure 7 Change of arterial wall radius (Rr) with transmural pressure (Pt)

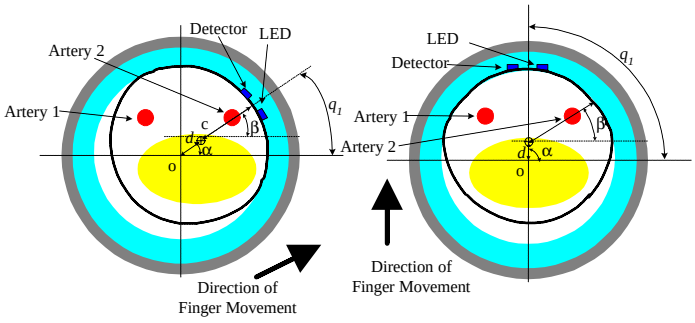

Figure 8 Two cases of finger movements in the ring

(a) Case 1 : $a = b = q_1$, $q_2 = 10^o$
(b) Case 2 : $a = q_1 = 90^o$, $q_2 = 10^o$

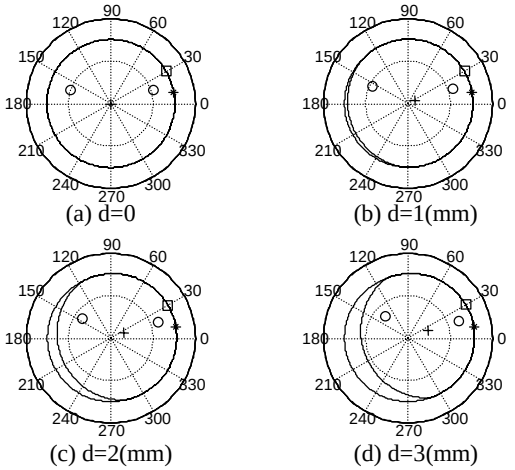

Figure 9 : Visualization of movement at case 1. It is shown that the finger shape becomes more oval as *d* increases.

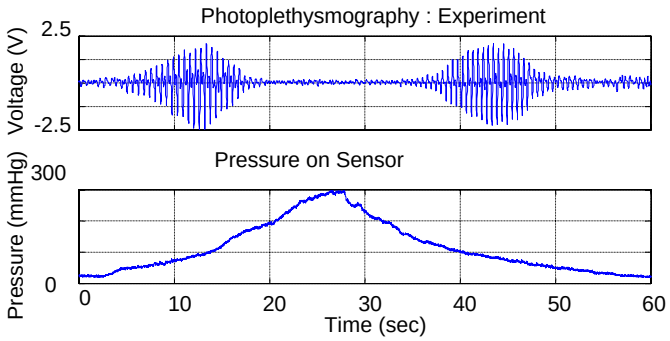

Figure 10 : Photoplethysmography and pressure at sensor unit from experiment in case 1

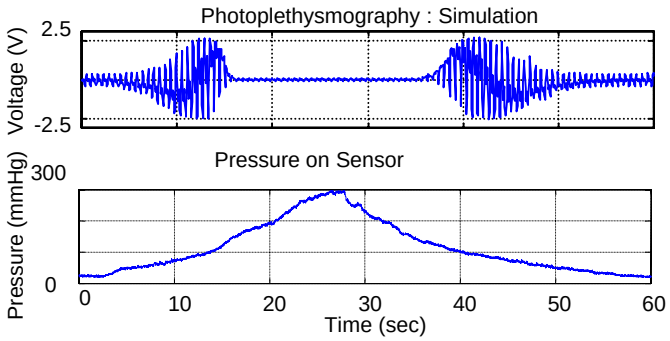

Figure 11 : Photoplethysmography and pressure at sensor unit from numerical simulation in case 1

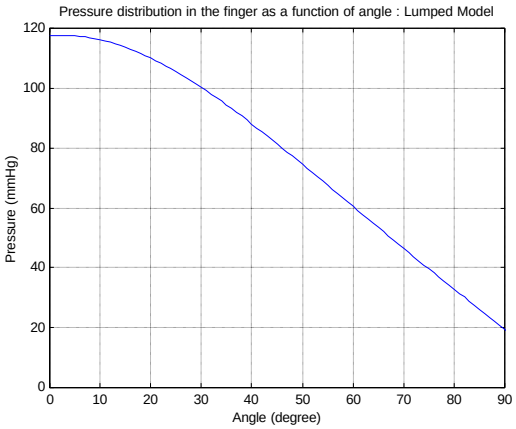

Figure 12 : Pressure distribution as a function of angle in the finger cross section generated by the lumped parameter model. The angle of displacement is 20 degree and displacement is 2 mm.

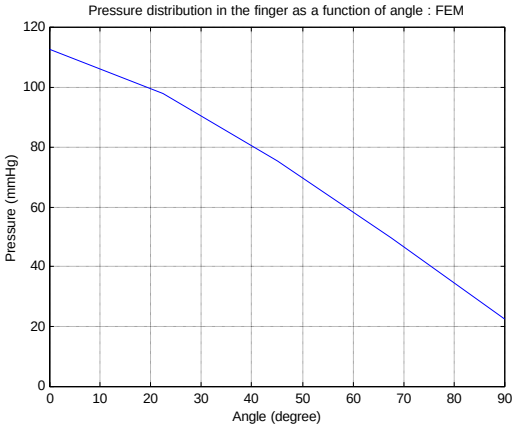

Figure 13 : Pressure distribution as a function of angle in the finger cross section generated by finite element method. The angle of displacement is 20 degree and displacement is 2 mm.

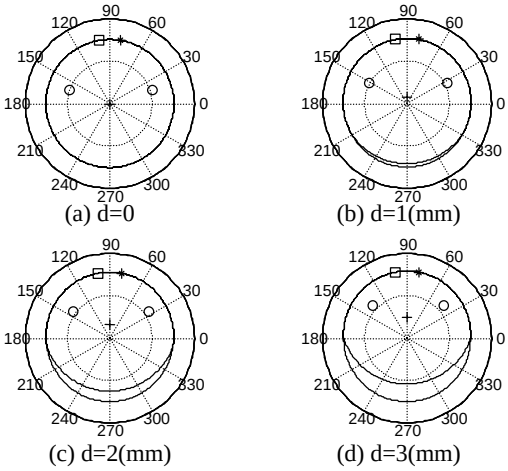

(a) d=0 (b) d=1(mm)

(c) d=2(mm) (d) d=3(mm)

Figure 14 : Visualization of movement at case 2. It is shown that the reference point (denoted as '+') moves toward the middle point of two arteries as *d* increases.

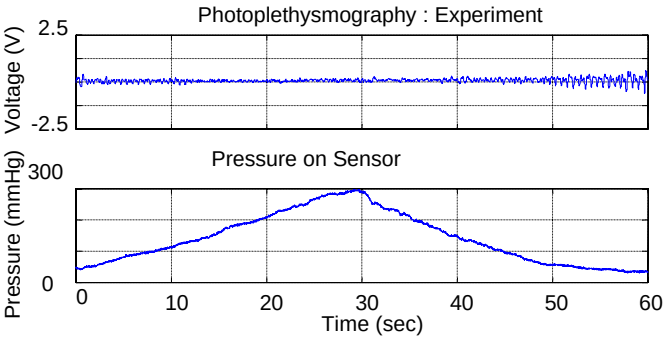

Figure 15 : Photoplethysmography and pressure at sensor unit from experiment in case 2

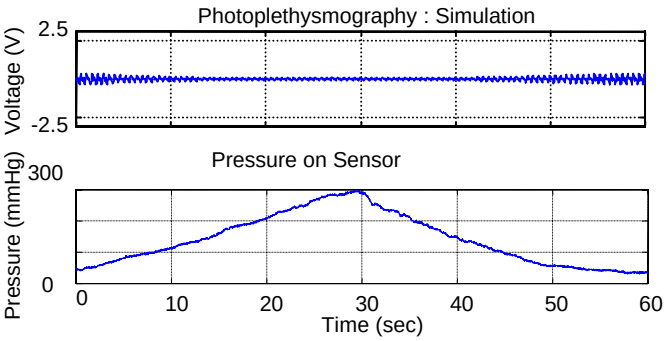

Figure 16 : Photoplethysmography and pressure at sensor unit from numerical simulation in case 2

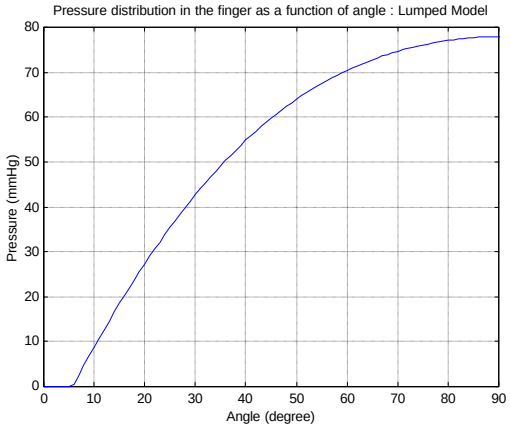

Figure 17 : Pressure distribution as a function of angle in the finger cross section generated by the lumped parameter model. The angle of displacement is 90 degree and displacement is 2 mm.

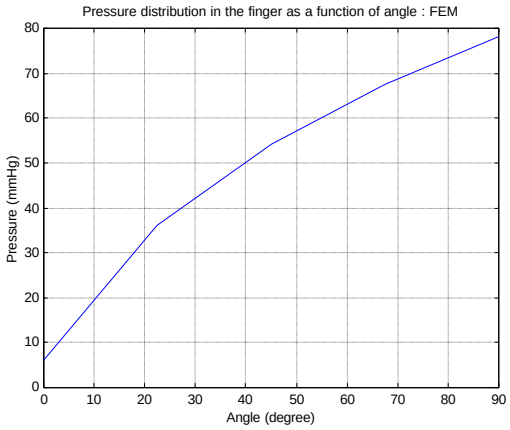

Figure 18 : Pressure distribution as a function of angle in the finger cross section generated by finite element method. The angle of displacement is 90 degree and displacement is 2 mm.

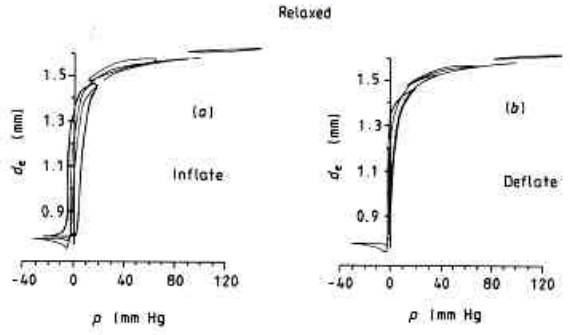

Figure 19 : Pressure-diameter relationship of human digital artery. The pressure in the x-axis is transmural pressure ($P_i - P_o$), and the y-axis is external diameter. The external diameter is about 0.8 mm at when it is completely collapsed, implying that the wall thickness at the collapse is about 0.4 mm. Adopted from [20]

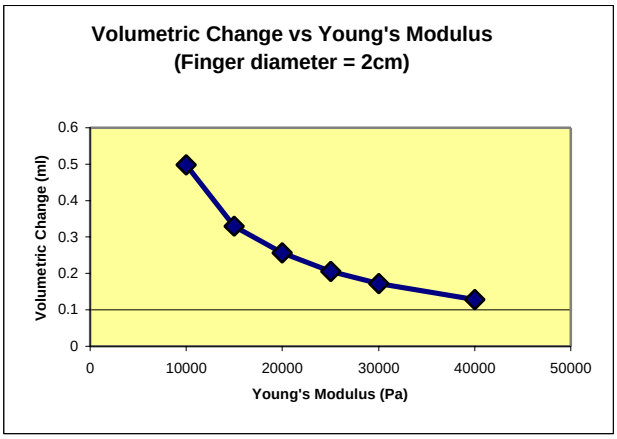

Figure 21 : Volumetric changes of the finger segment with various values for Young's modulus. The initial diameter of the finger segment is 2 cm, and its length is 1 cm.

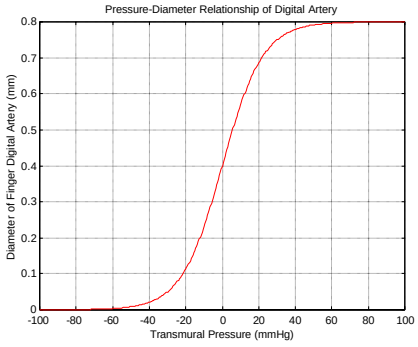

Figure 22 : Pressure-diameter relation curve described by sigmoid function. This curve was fitted to the experiment data in Figure [13].

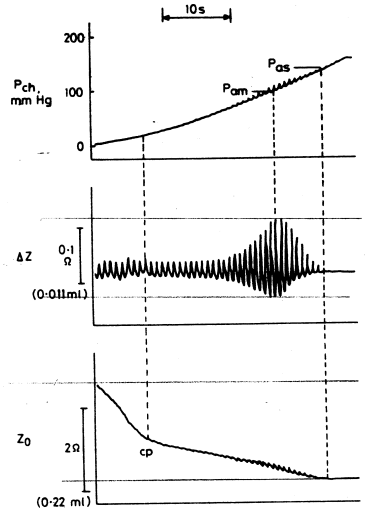

Figure 20 : Simultaneous recordings of chamber pressure (P_{ch}), AC components of impedance variation (DZ), and DC components of the impedance variation (Z_o). The impedance of the electrolyte solution decreases as the finger volume decreases. Adopted from [9].

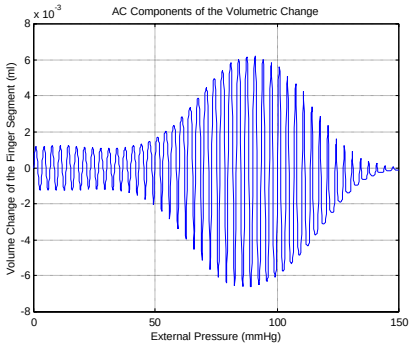

Figure 23 : Numerical simulation result of the volume change (AC components) of 1 cm finger segment under external pressure.

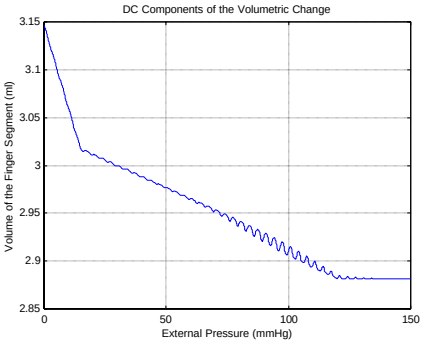

Figure 24 : Numerical simulation result of the volume change (DC components) of 1 cm finger segment under external pressure.

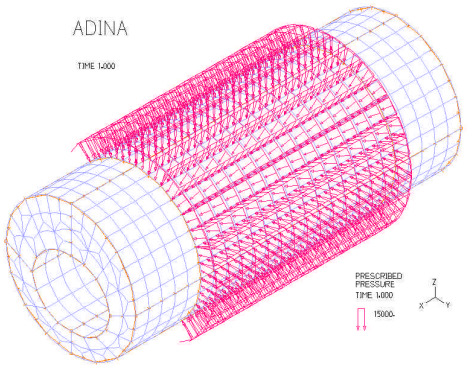

Figure 25 : Finite element analysis of the finger segment under constant pressure of 120 mmHg. The length of the finger of 4 cm, and 3cm segment is under the pressure.

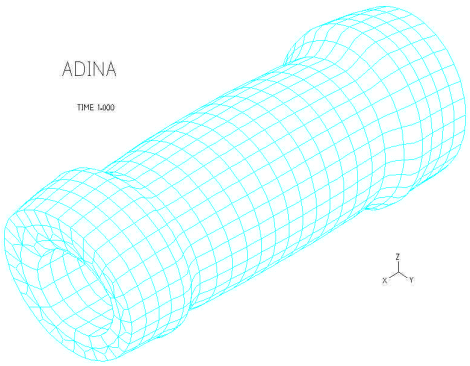

Figure 26 : Deformed finger segment under external pressure, generated by FEM.

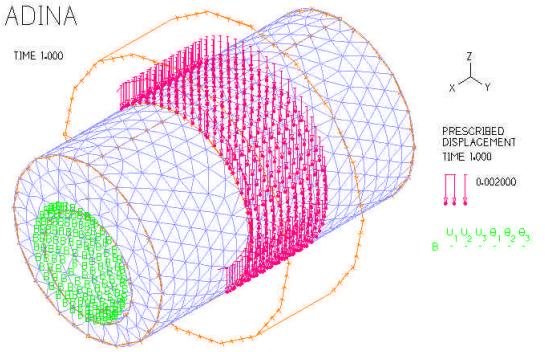

Figure 27 : FEM Analysis : Single Ring : E=20000, v=0.49, disp=2mm, angle=90 deg

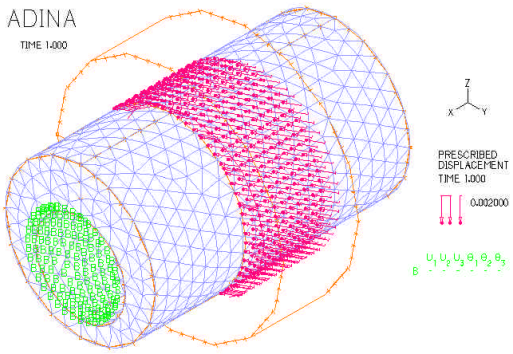

Figure 28 : FEM Analysis : Single Ring : E=20000, v=0.49, disp=2mm, angle=20 deg

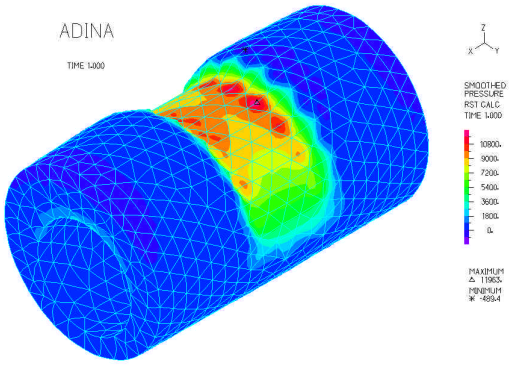

Figure 29 : Single Ring : E=20000, v=0.49, disp=2mm, angle=90 deg, 3-D View

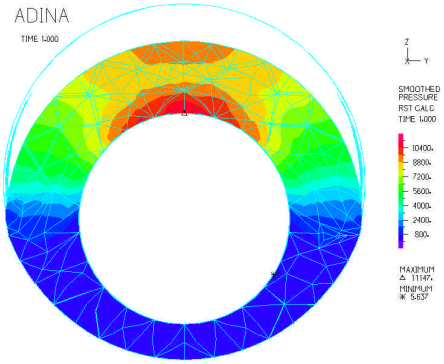

Figure 30 : Single Ring : E=20000, v=0.49, disp=2mm, angle=90 deg, Cross Sectional View at x=0

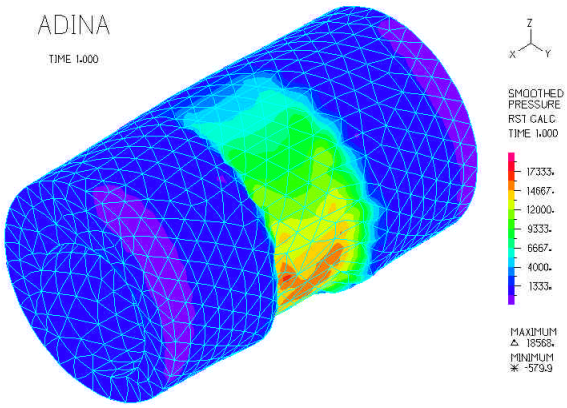

Figure 31 :Single Ring – 3-D View : E=20000, v=0.49, disp=2mm, angle=20 deg

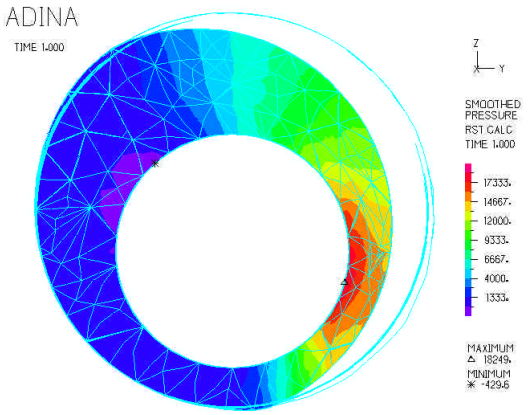

Figure 32 : Single Ring : E=20000, v=0.49, disp=2mm, angle=20 deg, Cross sectional view at x=0

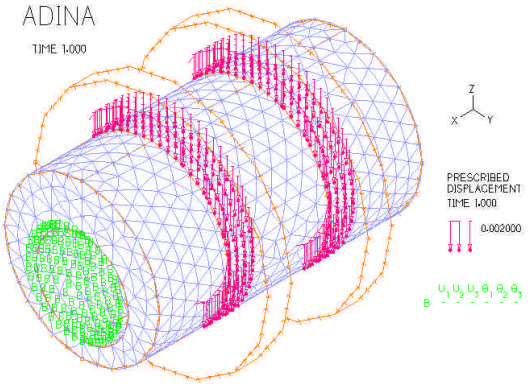

Figure 33 : FEM Analysis : Isolating Ring : E=20000, v=0.49, disp=2mm, angle=90 deg

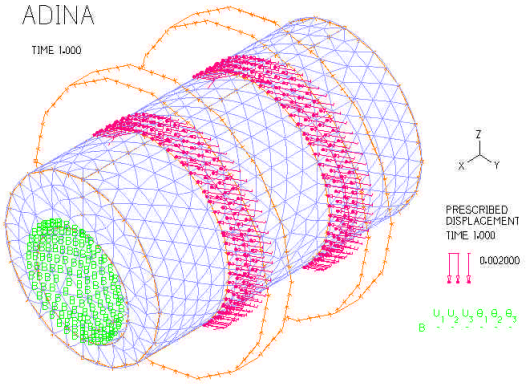

Figure 34 : FEM Analysis : Isolating Ring : E=20000, v=0.49, disp=2mm, angle=20 deg

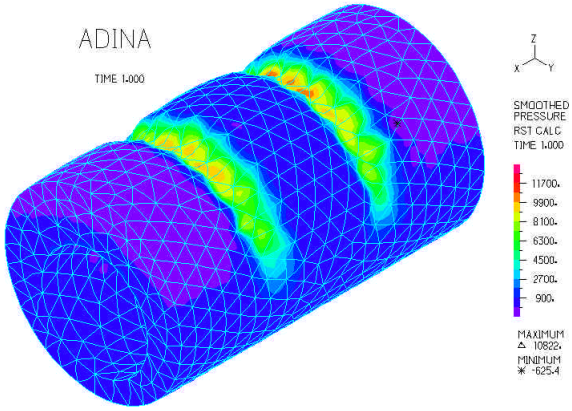

Figure 35 : Isolating Ring : E=20000, v=0.49, disp=2mm, angle=90 deg, 3-D View

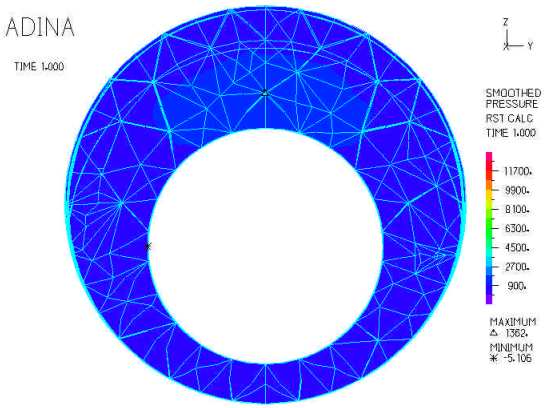

Figure 36 : Isolating Ring : E=20000, v=0.49, disp=2mm, angle=90 deg, Cross Sectional View at x=0

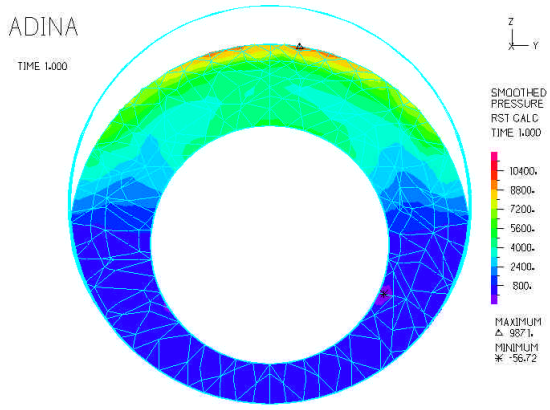

Figure 37 : Isolating Ring : E=20000, v=0.49, disp=2mm, angle=90 deg, Cross Sectional View at the Outer Ring

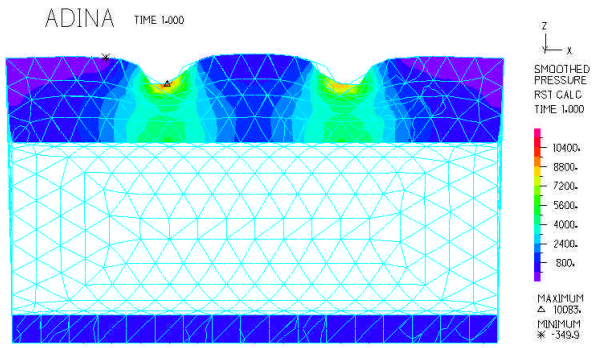

Figure 38 : Isolating Ring : E=20000, v=0.49, disp=2mm, angle=90 deg, Longitudinal View

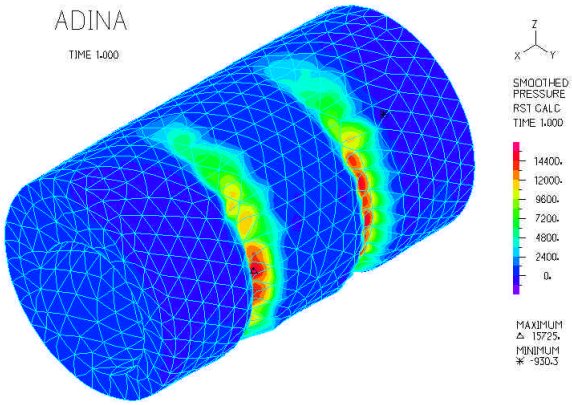

Figure 39 : Isolating Ring : E=20000, v=0.49, disp=2mm, angle=20 deg, 3-D View

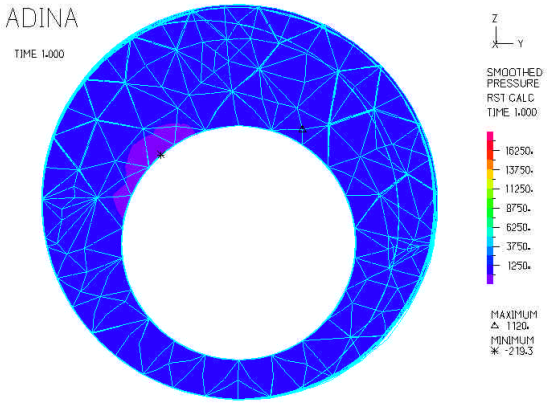

Figure 40 : Isolating Ring : E=20000, v=0.49, disp=2mm, angle=20 deg, Cross Sectional View at x=0

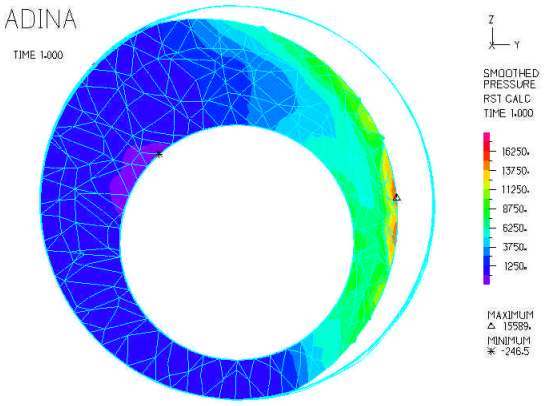

Figure 41 : Isolating Ring : E=20000, v=0.49, disp=2mm, angle=20 deg, Cross Sectional View at the Outer Ring

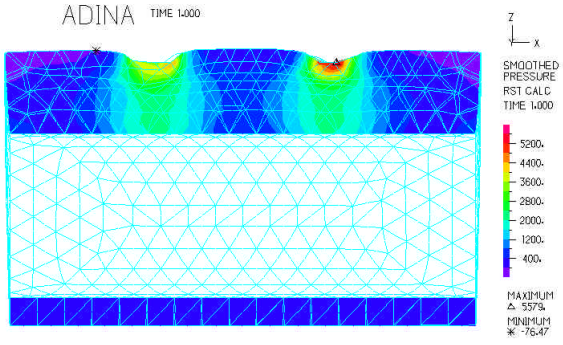

Figure 42 : Isolating Ring : E=20000, v=0.49, disp=2mm, angle=20 deg, Longitudinal Cut-Plane View

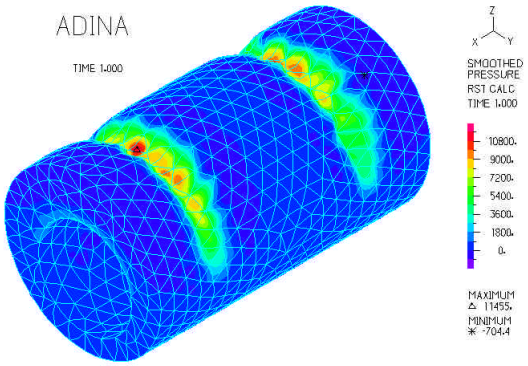

Figure 43 : Isolating Ring : E=20000, v=0.49, disp=2mm, angle=90 deg, Wide Ring, 3-D View

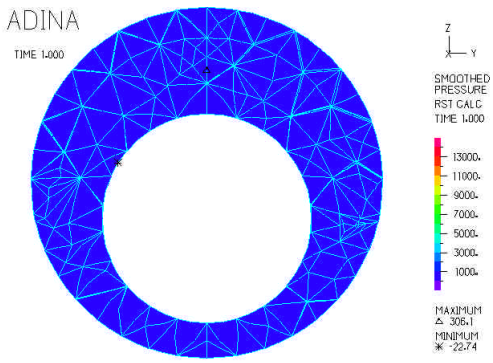

Figure 44 : Isolating Ring : E=20000, v=0.49, disp=2mm, angle=90 deg, Wide Ring, Cross Sectional View at x=0